Available online at www.sciencedirect.com
SCIENCE DIRECT®
Journal of Nuclear Materials 323 (2003) 181–191
journal of nuclear materials
www.elsevier.com/locate/jnucmat

MD modeling of defects in Fe and their interactions

Jaime Marian [a,*], Brian D. Wirth [a], Robin Schäublin [b], G.R. Odette [c], J. Manuel Perlado [d]

[a] Chemistry and Materials Science Directorate, Lawrence Livermore National Laboratory, 7000 East Avenue, Livermore 94550, USA
[b] CRPP, Fusion Technology and Materials, École Polytechnique Féderale de Lausanne, CK-5232, Villigen PSI, Switzerland
[c] Department of Mechanical Engineering, University of California, Santa Barbara, 1 Ward Memorial Dr., Santa Barbara, CA 93106, USA
[d] Instituto de Fusión Nuclear, Universidad Politécnica de Madrid, C/José Gutiérrez Abascal, 2, Madrid 28006, Spain

Abstract

Ferritic/martensitic steels considered as candidate first-wall materials for fusion reactors experience significant radiation hardening at temperatures below ~400 °C. A number of experimental studies in ferritic alloys, performed at higher temperatures, have shown the existence of large interstitial loops with Burgers vector $\frac{1}{2}\langle 1\,1\,1\rangle$ and $\langle 1\,0\,0\rangle$ in the bulk, which may provide a significant contribution to the hardening caused during irradiation at lower temperatures. Hardening arises from a high number density of loops, voids and small precipitates, which pin system dislocations, impeding their free glide. In this work, we review the nature of the different interstitial dislocation loops observed in α-Fe and ferritic materials, assess the effect of substitutional impurities on migrating $\frac{1}{2}\langle 1\,1\,1\rangle$ clusters, and apply atomistic modeling to investigate the mechanisms of formation and growth of $\langle 1\,0\,0\rangle$ loops from smaller cascade-produced $\frac{1}{2}\langle 1\,1\,1\rangle$ clusters. The proposed mechanism reconciles experimental observations with continuum elasticity theory and recent MD modeling of defect production in displacement cascades. In addition, the interaction of screw dislocations, known to control the low-temperature plastic response of b.c.c. materials to external stress, with $\langle 1\,0\,0\rangle$ dislocation loops is investigated with MD, where the main physical mechanisms are identified, cutting angles estimated and a first-order estimation of the induced hardening is provided.
© 2003 Elsevier B.V. All rights reserved.

PACS: 61.80.−x; 61.72.Ji; 61.82.Bg; 81.40.Lm

1. Introduction

Ferritic/martensitic steels are being considered as candidate first-wall materials for fusion reactors due to their excellent swelling resistance and low activation under neutron irradiation conditions [1,2]. However, the microstructural complexity of these steels, together with the extreme irradiation conditions under which they must perform, results in a wide range of observed radiation damage phenomena (creep, swelling, embrittlement) depending on the irradiation environment (temperature, dose, dose rate, etc.). For example, recent research in model alloys, has led to the identification of three temperature stages of radiation damage behavior [3]. At low temperatures, below ~400 °C, (i) the microstructure is dominated by a high number density of dislocation loops, resulting in radiation hardening of the material [4,5]. In the temperature range of approximately 450–800 °C, (ii) phenomena such as radiation creep and swelling appear [6,7]. At still higher temperatures, (iii) the presence of He from fusion and transmutation reactions

* Corresponding author. Address: Graduate Aeronautical Laboratories, MS: 205-45, California Institute of Technology, 1200 E. California Blvd., Pasadena, CA 91125, USA. Tel.: +1-626 395 8113; fax: +1-626 449 2677.
E-mail address: jaime@aero.caltech.edu (J. Marian).

0022-3115/$ - see front matter © 2003 Elsevier B.V. All rights reserved.
doi:10.1016/j.jnucmat.2003.08.037

leads to embrittlement through the formation of gas bubbles at inclusions and grain boundaries [8].

Hardening in the lower temperature regime is believed to arise from the formation of dislocation loops under irradiation that pin and may also decorate dislocations, thereby impeding their glide during deformation. A number of experimental studies performed over a wide range of temperatures in ferritic model alloys have shown the existence of large interstitial loops in the bulk, which may provide a significant contribution to the hardening caused during irradiation at lower temperatures [7]. The dislocation loops are observed with both $\frac{1}{2}\langle 1\,1\,1\rangle$ and $\langle 1\,0\,0\rangle$ Burgers vectors, although, generally, with a predominance of $\langle 1\,0\,0\rangle$ [9,10].

Numerous experimental observations [9–12] and atomistic simulation studies [13,14] have demonstrated the stability of both $\frac{1}{2}\langle 1\,1\,1\rangle$ and $\langle 1\,0\,0\rangle$ loops in ferritic materials. [1] Molecular dynamics (MD) simulations of high-energy cascades in Fe have revealed the formation of small, one-dimensionally mobile, $\frac{1}{2}\langle 1\,1\,1\rangle$ self-interstitial atom (SIA) clusters following the thermal spike stage of high-energy displacement cascades as a consequence of cooperative phenomena without long-range diffusion [13,15]. $\langle 1\,0\,0\rangle$ loops, on the other hand, have been recently proposed to form from the direct interaction of these small, cascade-produced, $\frac{1}{2}\langle 1\,1\,1\rangle$ clusters [11,16] and grow by the biased absorption of $\frac{1}{2}\langle 1\,1\,1\rangle$ loops to sizes visible by transmission electron microscopy (TEM), i.e. $\geqslant 2$ nm [16]. Therefore, the population of $\langle 1\,0\,0\rangle$ loops is directly related to the fate of $\frac{1}{2}\langle 1\,1\,1\rangle$ clusters produced in displacement cascades and, in this sense, the effect of impurities and solute atoms, or other foreign inclusions, on the formation, evolution and migration of these clusters may provide critical insight to the understanding of how the population of $\langle 1\,0\,0\rangle$ loops evolves as a function of the typical irradiation variables.

Nevertheless, $\frac{1}{2}\langle 1\,1\,1\rangle$ clusters are sub-nanometer in size and their detection by experimental means is limited by the time and spatial scales involved. In addition, the kinetics governing the nucleation and growth of $\langle 1\,0\,0\rangle$ loops occur over timescales that cannot easily be captured experimentally. From the atomistic perspective, the difficulty associated with MD studies is their lack of experimental confirmation resulting from the sample sizes that can be treated with the current computing capabilities, and the non-trivial relation between the dislocation loops generated with MD and their equivalent TEM images. This has led to the development of tools to investigate the correlation between defect structures produced by atomistic simulations and their observation in the TEM [17]. Thus, these tools partially bridge the gap existing between simulation and experimental observations and help in assessing experimental limitations in the observation of small defect clusters.

Ultimately, a high number density of dislocation loops in the appropriate temperature range can result in hardening by dislocation pinning, leading to a characteristic yield stress increase that can be measured experimentally using standard methods. In b.c.c. metals, screw dislocations dictate the plastic response at low temperatures and it is their behavior in the presence of irradiation-generated dislocation loops and the dynamics of their interactions that are key to understanding hardening in conditions relevant to fusion reactors. However, the atomistic nature of the interaction again makes these processes very difficult to study using conventional experimental techniques, whereas MD has been successfully applied to a number of scenarios involving different lattice defects and dislocations [18,19].

The purpose of this work is to address the aforementioned issues in a comprehensive manner from a computational perspective, using large-scale MD simulations with an emphasis on both the qualitative and quantitative aspects of the processes under study, i.e. identifying the operating mechanisms as well as extracting numerical information that will allow the quantification of the relevant magnitudes. This is done following a logical sequence of events, encompassing the pertinent time and space scales from the formation of small interstitial clusters in displacement cascades to determining the yield stress increase, useful for micromechanical estimations. All the MD simulations presented in this paper have been carried out with the MDCASK code [20] using the Fe–Cu potentials developed by Ackland and co-workers [21].

2. Formation and growth of $\langle 1\,0\,0\rangle$ loops in α-Fe

It is well established that examination of ferritic alloys by TEM following low dose rate irradiation to low doses (<0.1 dpa) by neutrons or heavy ions does not reveal any visible damage. However, as the irradiation dose increases above ~1 dpa, a significant population of prismatic dislocation loops, presumably of interstitial type, is experimentally observed [2] [9–12]. In contrast to other b.c.c. materials, such as Mo and V, the dislocation loops consist of Burgers vectors, $b\langle 1\,0\,0\rangle$ and $b = \frac{1}{2}\langle 1\,1\,1\rangle$, in almost equal proportions, rather than predominantly $\frac{1}{2}\langle 1\,1\,1\rangle$. A comparison of the dislocation loop energy based on continuum elasticity estimates (elastic energy proportional to Gb^2, where G is the shear modulus) indicates that $\frac{1}{2}\langle 1\,1\,1\rangle$ loops are energetically favored. Indeed, numerous MD studies of displacement

[1] As suggested by continuum elasticity theory.

[2] Recently, Nicol et al. [22] have observed $\langle 1\,0\,0\rangle$ dislocation loops in neutron irradiated samples at doses <0.1 dpa.

cascades in Fe show the formation of small SIA clusters that can coalesce within the cascade volume and form *proto* dislocation loops with $\frac{1}{2}\langle 1\,1\,1\rangle$ Burgers vectors that migrate in one dimension [14,15,23]. Thus, the observation of $\langle 1\,0\,0\rangle$ loops in α-Fe and other ferritic alloys has remained a puzzle for the last several decades, and although several mechanisms have been proposed to explain this disparity between theory and experiments, they are predicated on the existence of faulted loops (Eyre–Bullough mechanism [24]) or have only been observed in dislocation segments [25], and, therefore, are not plausible to describe the formation of $\langle 1\,0\,0\rangle$ interstitial loops in b.c.c. materials. Below, a mechanism that reconciles elasticity theory, MD simulations of displacement cascades in Fe and experimental observations in irradiated ferritic alloys is presented.

2.1. New mechanism of formation and growth of $\langle 1\,0\,0\rangle$ loops

The mechanisms of formation and growth of $\langle 1\,0\,0\rangle$ in α-Fe have been described in detail elsewhere [16] and are only briefly reviewed here. Several experiments in Fe and Mo performed in the early 1960s for a variety of loading conditions showed the formation of hexagonal dislocation networks composed of $\frac{1}{2}\langle 1\,1\,1\rangle$ and $\langle 1\,0\,0\rangle$ dislocation segments. The $\langle 1\,0\,0\rangle$ segments were presumed to form as a result of interactions, according to the reaction [11,16]:

$$\tfrac{1}{2}[1\,1\,1] + \tfrac{1}{2}[1\,\bar{1}\,\bar{1}] \rightarrow [1\,0\,0]. \quad (1)$$

In addition, this phenomenon has been recently observed in static computer simulations by Bulatov and Cai in Mo [26]. In 1965, Masters invoked reaction (1) to justify the observation of $\langle 1\,0\,0\rangle$ loops in thin-film ion irradiation studies [11]. However, Masters discounted the possibility of reaction (1) due to a lack of observed loops with $\frac{1}{2}\langle 1\,1\,1\rangle$ Burgers vector. Yet, such reactions can give rise to the formation of $\langle 1\,0\,0\rangle$ loops, especially with the widely accepted existence of $\frac{1}{2}\langle 1\,1\,1\rangle$ produced in cascades. Thus, in order to gain insight into this $\langle 1\,0\,0\rangle$-loop formation mechanism, we have performed a controlled MD simulation study of loop interactions associated with Eq. (1). The idea is to explore the configurational space (size, shape, etc.) within which these reactions do indeed occur.

Fig. 1 shows two different scenarios in which $\frac{1}{2}[1\,1\,1]$ and $\frac{1}{2}[1\,\bar{1}\,\bar{1}]$ interstitial clusters react with one another. In Fig. 1(a), a rhombic, 25-SIA, $\frac{1}{2}[1\,1\,1](1\,1\,0)$ and a hexagonal, 19-SIA, $\frac{1}{2}[1\,\bar{1}\,\bar{1}](1\,\bar{1}\,0)$ cluster with intersecting glide trajectories collide, driven by the reduction in elastic energy resulting from the high binding energy associated with interstitial clusters. Immediately after collision, a $[1\,0\,0]$ junction forms, consisting of three SIAs in the intersection boundary (white atoms). Another such interaction consisting of hexagonal and jogged hexagonal $\frac{1}{2}\langle 1\,1\,1\rangle$ loops with 37 and 34 interstitials, respectively, is shown in Fig. 1(b). Again, the initial condition is that both clusters have intersecting glide prisms. As in the previous case, a $[1\,0\,0]$ junction consisting of five SIAs on a $(1\,1\,0)$ plane formed instantaneously following the collision. Thorough analysis of many similar simulations reveals the necessary condition for $\langle 1\,0\,0\rangle$ junction formation in α-Fe; namely both interacting clusters need to be of approximately the same size, which must be larger than ~20 SIAs, have Burger's vectors in accordance with Eq. (1) and, possibly, have the same shape. When these constraints are not met, the smaller cluster is always observed to rotate into the $\langle 1\,1\,1\rangle$ orientation of the larger cluster, as has also been reported in other MD simulation studies [27].

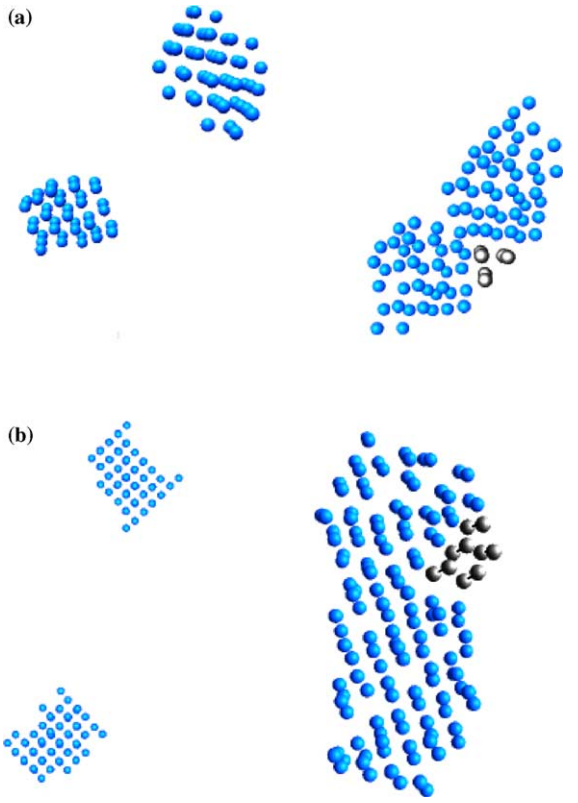

Fig. 1. (a) Two different MD snapshots of the interaction between a 19-SIA, hexagonal, $\frac{1}{2}[1\,1\,1](1\,1\,0)$ loop and a 25-SIA, rhombic, $\frac{1}{2}[1\,\bar{1}\,\bar{1}](1\,\bar{1}\,0)$ loop. On the left side of the image, 10 ps after the initiation of the simulation, the two loops are driven towards one another as a result of elastic interactions. After 45 ps, the loops collide forming a 3-SIA $[1\,0\,0]$ junction. (b) Similar case for two hexagonal $\frac{1}{2}\langle 1\,1\,1\rangle$ loops containing 37 and 34 interstitials. After 48 ps of dynamic simulation, the two loops interact forming a 5-SIA $[1\,0\,0]$ junction.

Nevertheless, the formation of the $\langle 1\,0\,0\rangle$ junction upon cluster interaction/collision is a kinetic process,

which does not necessarily imply its thermal stability. In the case shown in Fig. 1(b), after several hundred picoseconds at 1000 K, the junction grows throughout the resulting structure, gradually transforming it into a single entity with Burgers vector $b = \langle 1\,0\,0\rangle$ [16,28]. In terms of dislocation reactions, we have seen that these $\frac{1}{2}\langle 1\,1\,1\rangle$ loop interactions display an important property, i.e. that the glide direction of each one of the reacting loops is contained in the other's habit plane. This means that, once the loops collide and the $\langle 1\,0\,0\rangle$ junction is formed, the perturbation (no mass transport) brought by one loop transmits throughout the other, and vice versa, in the form of shear dislocations of the $\frac{1}{2}\langle 1\,1\,1\rangle$ type. This results in reactions like (1), transforming the Burgers vector to $\langle 1\,0\,0\rangle$ as is illustrated schematically in Fig. 2. At the atomic level, the junction is seen to propagate by individual self-interstitial atoms according to the two-step reaction:

$$\begin{aligned} &\tfrac{1}{2}[1\,1\,1] + \tfrac{1}{2}[0\,0\,\bar{1}] \rightarrow \tfrac{1}{2}[1\,1\,0],\\ &\tfrac{1}{2}[1\,1\,0] + \tfrac{1}{2}[1\,\bar{1}\,0] \rightarrow [1\,0\,0], \end{aligned} \tag{2}$$

which is a variation of the original Eyre–Bullough mechanism referred to earlier [24]. The first reaction in Eq. (2) requires an activation energy of ~0.5 eV (see schematic energy landscape in Fig. 3), whereas the second requires much higher energies, of the order of 1.0 eV. This energy landscape reveals that the $\frac{1}{2}\langle 1\,1\,1\rangle$-to-$\langle 1\,0\,0\rangle$ path of the reaction is more favorably sampled than the inverse $\langle 1\,0\,0\rangle$-to-$\langle 1\,1\,0\rangle$-to-$\langle 1\,1\,1\rangle$ path (which

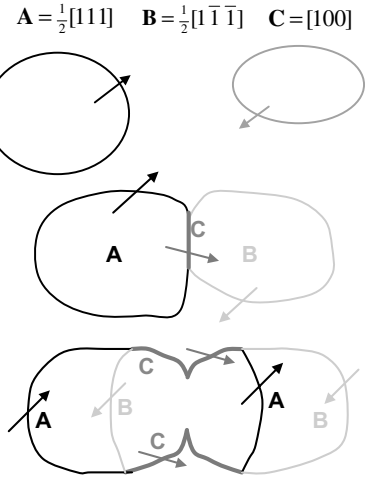

Fig. 2. Schematic representation of the interaction between two $\frac{1}{2}\langle 1\,1\,1\rangle$ loops with Burgers vectors given by Eq. (1) (A and B). When the loops collide, a $\langle 1\,0\,0\rangle$ segment (C) forms. If the glide directions (A and B) of the original loops are contained in each other's habit planes, during the subsequent annealing A- and B-type shear dislocations complementarily propagate through the loops, giving rise to C-type segment growth.

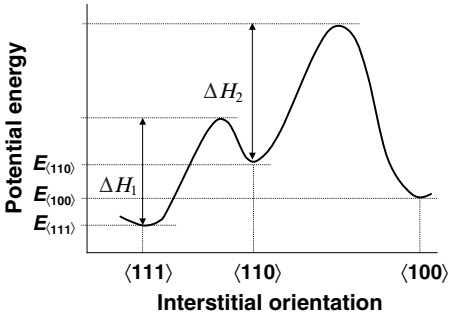

Fig. 3. Schematic energy landscape of reaction (2) extracted from static calculations. Interstitials with a $\langle 1\,1\,1\rangle$ orientation readily rotate into and out of a metastable $\langle 1\,1\,0\rangle$ orientation with an activation energy, $\Delta H_1 \approx 0.5$ eV. Occasionally, SIAs go over the second energy barrier, $\Delta H_2 \approx 1.0$ eV, into a $\langle 1\,0\,0\rangle$ orientation, where they become kinetically trapped due to the intrinsic difficulty to go along the inverse energy path (energies >1.0 eV). This results in an effective $\frac{1}{2}\langle 111\rangle$-to-$\langle 100\rangle$ loop transformation.

requires energies >2.0 eV). Over prolonged timescales, we project that this leads to an effective $\frac{1}{2}\langle 1\,1\,1\rangle$-to-$\langle 1\,0\,0\rangle$ loop transformation. In principle, the partial concentrations in thermodynamic equilibrium are solely dictated by the energy difference between $\frac{1}{2}\langle 1\,1\,1\rangle$ and $\langle 1\,0\,0\rangle$ loops ($E_{\langle 1\,1\,1\rangle} - E_{\langle 1\,0\,0\rangle}$ in Fig. 3), which suggests ~50% relative proportions for large sizes [16], although the kinetics of the reaction [3] favors the formation of $\langle 1\,0\,0\rangle$ loops rather than their dissolution. This explains why, in a certain temperature range, $\langle 1\,0\,0\rangle$ loops, although higher in energy (as discussed in detail in Ref. [16]), are more readily observed than $\frac{1}{2}\langle 1\,1\,1\rangle$.

The remaining point to consider is how $\langle 1\,0\,0\rangle$ clusters grow to TEM observable sizes. Although intrinsically glissile owing to their pure-edge prismatic nature, the b.c.c. crystal structure dictates that $\langle 1\,0\,0\rangle$ $\{100\}$ loops require a large jump distance of a_0. This results in a very high migration energy, computed to be >2.5 eV. Thus, once formed, $\langle 1\,0\,0\rangle$ loops are essentially stationary, and become a biased-sink for mobile, cascade-produced $\frac{1}{2}\langle 1\,1\,1\rangle$ loops. Notably, MD simulations of interactions between $\frac{1}{2}\langle 1\,1\,1\rangle$ $\{1\,1\,0\}$ and $\langle 1\,0\,0\rangle$ $\{1\,0\,0\}$ loops reveal $\langle 1\,0\,0\rangle$ loop growth in this manner [16], resulting in TEM-visible loops (>2 nm).

In any case, the effective cross-section for $\langle 1\,0\,0\rangle$ loops to form is intrinsically low (as corresponds to a reaction so highly constrained geometrically and configurationally) and depends heavily on the migration properties of $\frac{1}{2}\langle 1\,1\,1\rangle$ clusters. Factors such as impurity trapping, enhancement of 3D diffusion due to solute/microstructure interactions, and high dose rate can significantly enhance the collision probability of 1D-migrating $\frac{1}{2}\langle 1\,1\,1\rangle$

[3] Together with the 1D nature of $\frac{1}{2}\langle 1\,1\,1\rangle$-cluster migration.

defects and contribute to the formation of $\langle 1\,0\,0\rangle$ loops. It has been suggested that $\langle 100\rangle$ loops could form from two $\frac{1}{2}\langle 1\,1\,1\rangle$ clusters originating in the same cascade event provided that the energy density in the cascade volume is sufficiently high, but there is no direct evidence to support this and only vacancy loops have been directly observed to form in MD simulations of very high energy (>50 keV) cascades in Fe [29]. In the following section, we analyze the effect of oversized substitutional impurities on the migration properties of $\frac{1}{2}\langle 1\,1\,1\rangle$ interstitial clusters.

2.2. Dynamics of SIA clusters in pure Fe and dilute Fe–Cu alloys

The interest of considering Cu as a perturbing substitutional solute on SIA cluster migration is twofold. First, Cu is known to precipitate in nuclear reactor pressure vessel steels, leading to embrittlement, and, although not so important for fusion, its technological importance is well recognized. Second, Cu is one of the most widely studied metals in condensed matter physics, and for which a number of reliable semi-empirical potentials have been developed. Notably, there have been very few modeling studies which take into account the effect of alloy elements on crystal and defect properties and thus, in this work, we seek to generalize the effect of Cu on crystal and defect properties to all substitutional impurities in the Fe matrix in terms of elastic interactions, i.e. ignoring electronic contributions.

The interactions of concern in this study involve the effect of individual Cu substitutional solute atoms on the migration behavior of $\frac{1}{2}\langle 1\,1\,1\rangle$ SIA clusters. The idea is to compare the diffusion pre-factors, D_0, and migration energies, E_m, of $\frac{1}{2}\langle 1\,1\,1\rangle$ clusters as a function of the cluster size, n, in pure α-Fe and in a dilute Fe–1.0 at.% Cu alloy. The study is aimed not only at identifying the governing interaction mechanisms but also at extracting physically-based extrapolation laws that allow us to express either D_0 or E_m, as a non-linear function of n.

The details of this study have been previously published for single SIAs [30] and SIA clusters [31] and thus, only its main conclusions are outlined here. In general, the interactions between Cu atoms and SIA-type defects can be described in terms of the interactions between the atomic displacement fields around each type of defect. For single interstitials, the interaction can be repulsive or attractive (characterized by negative or positive binding energies) depending on the position of the spherically symmetric displacement field of a Cu atom relative to the fourfold symmetric, anisotropic field of the interstitial. Negative interactions induce rotations of the SIA to attain slightly positively bound (~0.02–0.04 eV) Cu–SIA configurations, thereby effectively providing a boost to overcome the rotational energy barrier and resulting in a reduced effective activation energy for single SIA migration with respect to pure Fe [32]. We also observe this effect on small ($n < 4$) clusters, which exhibit 3D mobility during typical MD simulations. The overall effect is an enhancement of the 3D character of the migration of small self-interstitial clusters ($n < 5$).

For larger clusters, which only exhibit 1D motion during typical MD simulations, there is no appreciable change in the temperature dependence of the calculated cluster diffusivity. However, the absolute magnitude of the diffusion pre-factor, D_0, does decrease in the Fe–Cu alloy. This can be attributed to a reduced jump attempt frequency in the $\langle 1\,1\,1\rangle$ direction and is an entropic effect, which results from Cu atoms positioned perpendicularly to the migration trajectory. This again enhances the 3D nature of the clusters' migration and reduces the relative length of the $\langle 1\,1\,1\rangle$ correlated trajectories of larger clusters.

The migration energies and diffusion pre-factors are plotted against cluster size in Fig. 4, where 3D and 1D regimes are distinguished. The resulting curves have been fitted to physically based quantitative extrapolation laws which take the following form in pure α-Fe [31]:

$$\begin{aligned} E_m(n) &= 0.06 + 0.07n^{-1.3}\ (\mathrm{eV}),\\ D_0(n) &= 8.98\times 10^{-3} n^{-0.61}\ (\mathrm{cm^2\,s^{-1}}), \end{aligned} \tag{3}$$

and in Fe–1.0 at.% Cu:

$$\begin{aligned} E_m(n) &= 0.05 + 0.04n^{-3.1}\ (\mathrm{eV}),\\ D_0(n) &= 5.07\times 10^{-3} n^{-0.74}\ (\mathrm{cm^2\,s^{-1}}). \end{aligned} \tag{4}$$

One important conclusion of this study is the enhanced nature of 3D-migration of $\frac{1}{2}\langle 1\,1\,1\rangle$ clusters as a result of interactions with oversized substitutional Cu solute atoms, which, when considered in accordance with the reduced diffusion pre-factors, D_0, could lead to an increased $\frac{1}{2}\langle 1\,1\,1\rangle$-cluster reaction cross-section. Clearly, $\langle 1\,0\,0\rangle$ loop formation, would be increased from an increase in $\frac{1}{2}\langle 1\,1\,1\rangle$-loop reaction cross-sections and it is reasonable to expect that such an increase would be much larger for interstitial (octahedral) rather than for substitutional solute/impurities, like the ones studied in this work. In fact, there is experimental evidence suggesting such a possibility [33]. In any case, the reactions and numerical laws presented in Sections 2.1 and 2.2 can now be incorporated into longer-scale, kinetic Monte Carlo (kMC) or rate theory models with the purpose of exploring the long term damage accumulation and microstructural evolution required to calculate defect concentrations in irradiation conditions.

2.3. TEM image simulations

The computational and theoretical study presented above can be substantially strengthened through validating

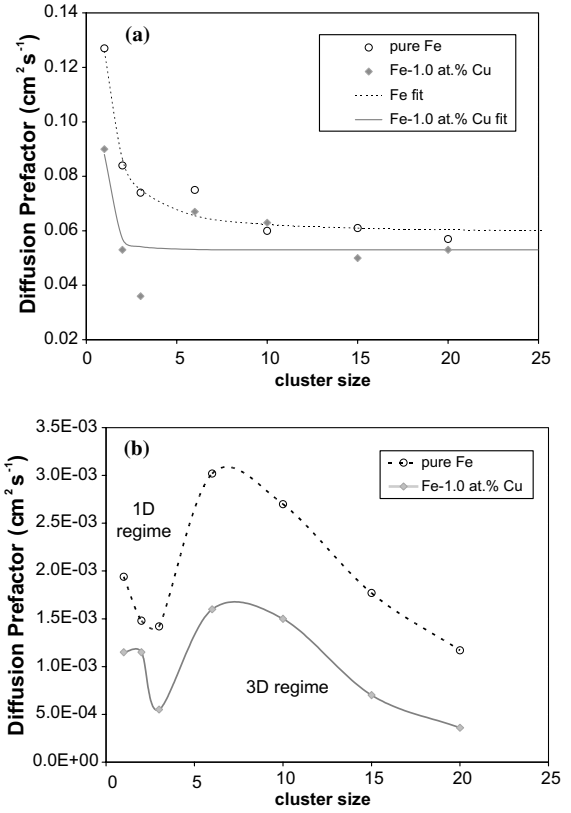

Fig. 4. (a) SIA cluster migration energies, and respective non-linear fits, as a function of cluster size n in pure Fe and in Fe–1.0 at.% Cu. In both cases, E_m approaches the asymptotic value of the $\langle 1\,1\,1\rangle$, size-independent, migration step. For low cluster sizes, the value of E_m includes the rotation activation barrier, which significantly increases the total migration energy value. (b) Diffusion pre-factors as a function of size. The marked drop in the curves for about $n \sim 3$–4 denotes the transition from 3D to 1D migration. The pre-factors tend to zero as the cluster size becomes sufficiently large to form dislocation networks that do not move in the absence of an applied stress.

the key conclusions with direct comparison with experimental results. There are two possible ways of contrasting the results obtained by numerical simulation: (i) comparing the normalized number densities and size distributions of $\langle 1\,0\,0\rangle$ (and $\frac{1}{2}\langle 1\,1\,1\rangle$) loops in identical conditions – quantitative comparison – and (ii) comparing the structure of the defects obtained by way of atomistic simulation with real TEM micrographs – qualitative comparison. The former case has been preliminarily presented by Caturla et al. [34] using kMC, while the latter type of comparison has been performed by Marian et al. [35] and is briefly reviewed below.

The conventional TEM (CTEM) images of the dislocation loops are simulated using the multislice method to obtain their weak-beam image at 200 kV. This is performed with the EMS software package [36]. Ideally, for CTEM, and more precisely for weak-beam image simulations, the sample ought to be more than 10-nm thick to avoid surface effects, and thinner than 80 nm to reduce anomalous absorption, which arises from inelastic scattering of the electrons, that would result in a blurry image. Details on the main elements of the approach are given elsewhere [35,37]. The sample obtained from MD simulations is cut perpendicular to the electron beam direction in slices 0.2-nm thick. The sample is in all cases cut into 100 slices that are roughly 10 nm on a side and contain approximately 2000 atoms. In this case, the diffraction vector was picked to be $\mathbf{g} = (200)$ and the diffraction condition was $\mathbf{g}(4.1\mathbf{g})$. The parameters used to obtain the images are similar to those of modern microscopes operated at an acceleration voltage of 200 kV.

CTEM simulated images of a number of large (4–18 nm) loops were obtained to allow direct comparison with experiments. Fig. 5 shows an experimental TEM, weak beam, $\mathbf{g}(4.1\mathbf{g})$, $\mathbf{g} = (2\,0\,0)$ image of a Fe–9Cr tempered martensitic steel sample irradiated at high dose rate and 302 °C, up to a total dose of 8.8 dpa. The observed microstructure contains a number of features, most of which are defect structures generated by the irradiation. The two insets displayed in Fig. 5 represent the simulated TEM image of an 18-nm long, 937-SIA,

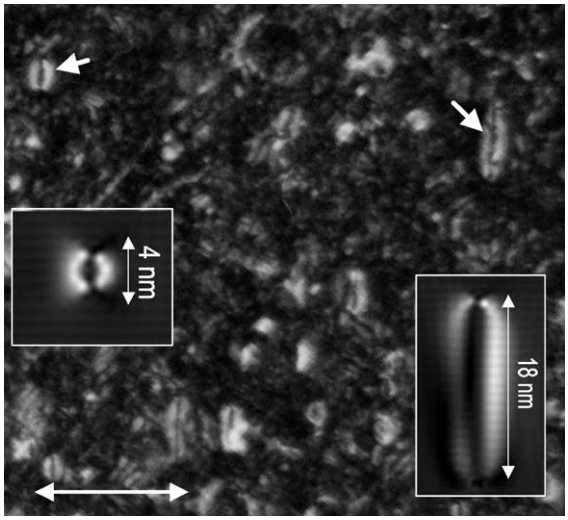

Fig. 5. Experimental TEM weak beam image of a Fe–9Cr crystal irradiated with neutrons to a dose of 8.8 dpa at 302 °C. The two insets represent TEM simulated images of an 18-nm, rectangular [1 0 0] loop and a 4-nm, hexagonal, [1 0 0] loop. A number of features can be observed in the TEM micrograph, among which two (pointed by arrows) interstitial loops with Burgers vector [1 0 0], sitting on {1 0 0} planes, can be identified. The qualitative agreement with the simulated loops in both contrast and shape is excellent.

rectangular, $\langle 1\,0\,0\rangle$ $\{1\,0\,0\}$ loop (A – bottom right) and a 5 nm, 91-SIA, hexagonal, $\langle 1\,0\,0\rangle$ $\{1\,0\,0\}$ loop (B – top left). Both loops exhibit double-*bean* black-and-white contrast and other characteristics that can be qualitatively recognized in the experimental micrograph, where two defects with similar size and contrast have been pointed out (A and B). These are interstitial dislocation loops with $\langle 100\rangle$ Burgers vector and lying on $\{1\,0\,0\}$ planes. We emphasize the excellent qualitative agreement between the simulations and the experimental observations. These results suggest that the structure of $\langle 1\,0\,0\rangle$ $\{1\,0\,0\}$ loops simulated with MD correlates very well with experimental observations, which further substantiates the whole approach explained in Section 2.

3. Estimation of the hardness due to $\langle 1\,0\,0\rangle$ loops

Based on Orowan's simple model, the most commonly used expression for the change in shear stress, $\Delta\tau_s$, induced in the dislocation glide plane by a regular array of defects is given in the following equation:

$$\Delta\tau_s = \alpha G b (Nd)^{1/2}, \tag{5}$$

where G is the shear modulus, b the Burgers vector of the dislocations, N the defect number density, d the defect diameter and the square-root factor is the reciprocal of the average distance between obstacles. The α factor in Eq. (5) is known as the obstacle strength and is determined as $\alpha = \cos(\theta/2)$, where θ is the angle in the line tension approximation at which the dislocation is able to break through the obstacle and continue its glide (for an impenetrable object $\theta = 0$, $\alpha = 1$). However, relatively few measurements of the critical angle have been made for radiation-induced defects and, in practice, microstructural observations and mechanical property measurements are compared to infer values of α for different types of defects [38]. Atomistic simulations provide a direct calculation of the dislocation–obstacle interaction and critical bowing angle, which, together with other simulation methods, can provide all of the required input to Eq. (5). The computational elements necessary for this type of calculations are: (i) generation of a screw dislocation, (ii) introduction of an appropriate obstacle (e.g. a $\langle 1\,0\,0\rangle$ loop), and (iii) the development of the capability to reproduce the conditions required for the interaction (i.e. temperature, stress, etc.). In what follows, we provide a self-consistent computational framework based on MD simulations to obtain an approximate value of $\Delta\tau_s$.

3.1. Generation of a screw dislocation in α-Fe

The isotropic linear elasticity solution corrected with image summations for periodic boundary conditions is used to introduce a screw dislocation dipole into an otherwise perfect crystallite. In general, the introduction of a dipole, which is a measure intended for conserving the periodicity of the crystal, is not an appropriate initial condition for the simulations, as the dynamics of both dislocations are characterized by a strong self-annihilating bias. In order to remove one of the dislocation poles, the box must be cut accordingly, i.e. several atomic layers must be removed. This eliminates the periodicity in at least one direction, which further requires the use of appropriate boundary conditions. The computational boxes employed in this study were $100 \cdot a_0\frac{\sqrt{3}}{2} \times 40 \cdot a_0\sqrt{6} \times 50 \cdot a_0\sqrt{2}$, which amount to about 10^6 atoms. In general, for these large-scale simulations, flexible boundary conditions in the form of free surfaces have been used. These free surfaces have been generated in a way that is appropriate to the application of a desired shear stress in the computational box. After cutting the box to generate the free surfaces, the dislocation density is computed to be $\rho = 2.9 \times 10^{15}$ m^{-2}. Prior to any external application of stress, a relaxation of the linear-elastic dislocation configuration is performed at zero stress and a temperature-controlled equilibration at the target temperature. The stress (or more appropriately a surface traction) is applied on a skin region corresponding to the outermost atomic layers (one to three) adjacent to the free surfaces. The character and direction of the bounding surfaces and applied stress are considered concurrently to obtain the desired Peach–Köhler force (generally on $\{1\,1\,0\}$ and $\{1\,1\,2\}$ glide planes). In addition to this externally induced force, image forces result from the existence of the traction-controlled (free) surfaces. These, together with the directional bias towards twinning orientations, are the sole forces exerted on the dislocation and upon which the dynamics of its motion are studied.

3.2. Dislocation–obstacle interaction

The above knowledge of the dynamic constraints is required to appropriately position the obstacle in the presumed path of the dislocation. The obstacle was chosen to be a $[1\,0\,0](1\,0\,0)$ dislocation loop with rhombic shape containing 113 interstitials (~2 nm). A shear stress of 750 MPa was applied to the crystallite containing both the screw dislocation and the loop at a temperature of 100 K. Since the applied stress is below the computed Peierls stress (900 MPa for this potential), the dislocation begins to glide by a double-kink mechanism on $\{1\,1\,0\}$ planes. Two out of the eight possible $\{1\,1\,0\}$ planes become activated and the dislocation performs a serrated glide, generating kinks on both planes as well as on one $\{1\,1\,2\}$ plane in the twinning sense, thus effectively moving on an 'apparent' single $\{1\,1\,2\}$ plane. In these simulations, the loop is also subject to the applied stress and undergoes several

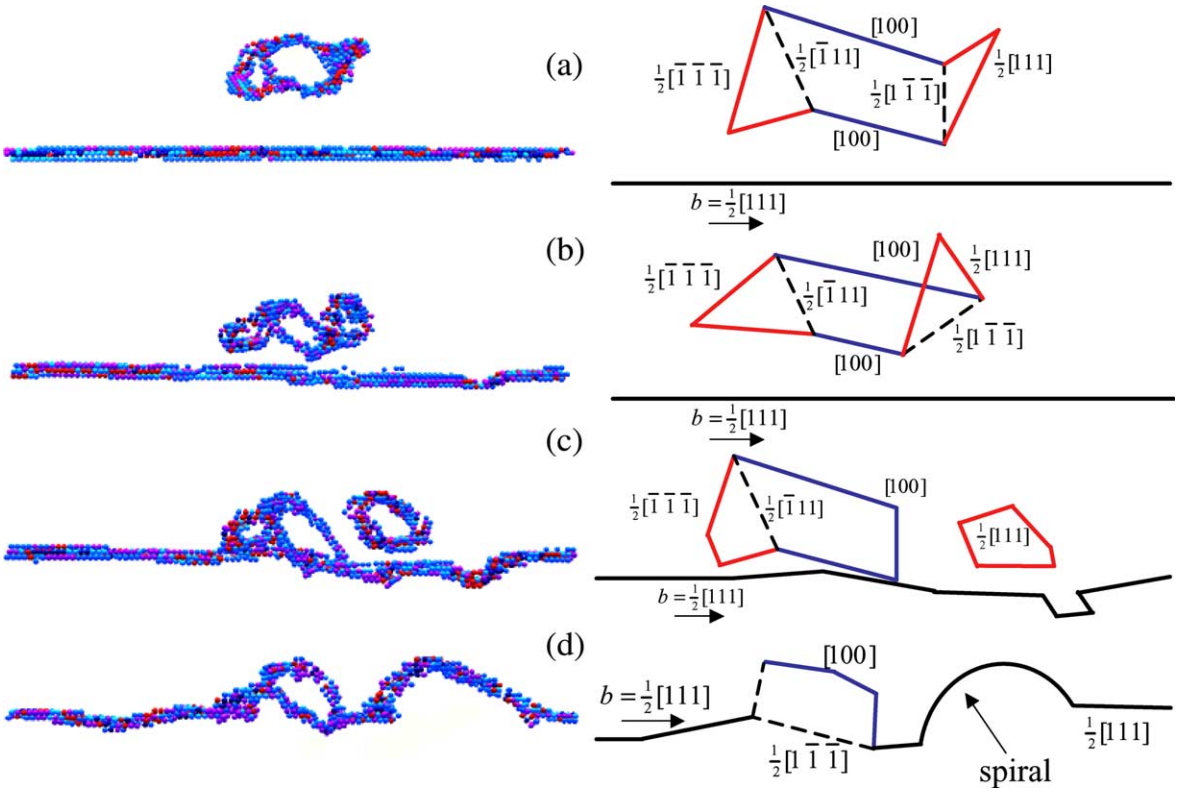

Fig. 6. Sequence of MD snapshots (left) and equivalent dislocation interpretation (right) of the interaction between a 113-SIA, rhombic [1 0 0] dislocation loop and a $\frac{1}{2}[1\,1\,1]$ screw dislocation at 100 K and 750 MPa of applied shear stress. The dislocation and loop cores have been visualized using the centro-symmetry deviation parameter [28]. The identification of the Burgers vectors for both the screw dislocation and the SIA loop was done using a 3D Burgers-circuit analysis. Details of the interaction are given in the text.

structural transformations prior to interacting with the dislocation. The whole process is illustrated in Fig. 6. The loop's corners initially transform into $\frac{1}{2}\langle 1\,1\,1\rangle$ segments by way of Eq. (1) (Fig. 6(a)). In Fig. 6(b), the right corner of the loop is subject to secession forces as the dislocation comes closer. This is a combination of multiple factors. First, the applied external and the dislocation stress fields superimpose to exert a force on the loop corners with $\frac{1}{2}\langle 1\,1\,1\rangle$ geometry. Second, due to their prismatic nature, these $\frac{1}{2}\langle 1\,1\,1\rangle$ segments are amenable to thermally activated diffusion along the direction of the dislocation line. Indeed, in Fig. 6(c) a perfect $\frac{1}{2}[1\,1\,1]$ loop is emitted from the right section of the parent dislocation loop. At this point, the screw dislocation continues to move by a double-kink mechanism until it comes into contact with the central [1 0 0] section of the original loop. Finally, Fig. 6(d) shows the absorption of both the emitted loop (right side of the interaction) and the remaining $\frac{1}{2}\langle 1\,1\,1\rangle$ corner situated at the left side. In both cases, heavily arched, spiral segments of different dimensions are generated, leaving a central section consisting of a [1 0 0] loop and a pinned $\frac{1}{2}[1\,1\,1]$ screw dislocation. In all cases, the Burgers vectors of the different screw dislocation and dislocation loop segments were determined by way of a 3D Burgers circuit analysis.

The entire interaction process lasted for 150 ps (at strain rates of the order of $\dot{\varepsilon} \approx 1.4 \times 10^8$ s^{-1}) but, after 200 ps of annealing, the dislocation remained pinned and the only remarkable observation was the elastic transmission of the spiral (stretching) along the dislocation line. An increase in the applied shear stress was required to force the screw dislocation through the pinning obstacle.

3.3. Estimation of the hardening

The stress was gradually increased and applied to the pinned structure described above in 50 MPa increments. Only after a value of 1.0 GPa was the screw dislocation able to traverse the [1 0 0] loop. This increment in the external stress (250 MPa) is already a first-order estimate of the value of $\Delta\tau_s$. The dislocation starts to bow around the dislocation loop until, for $\theta \approx 70°$, it can finally surpass the obstacle and continue with its normal unconstrained glide. Fig. 7 shows the last snapshot before

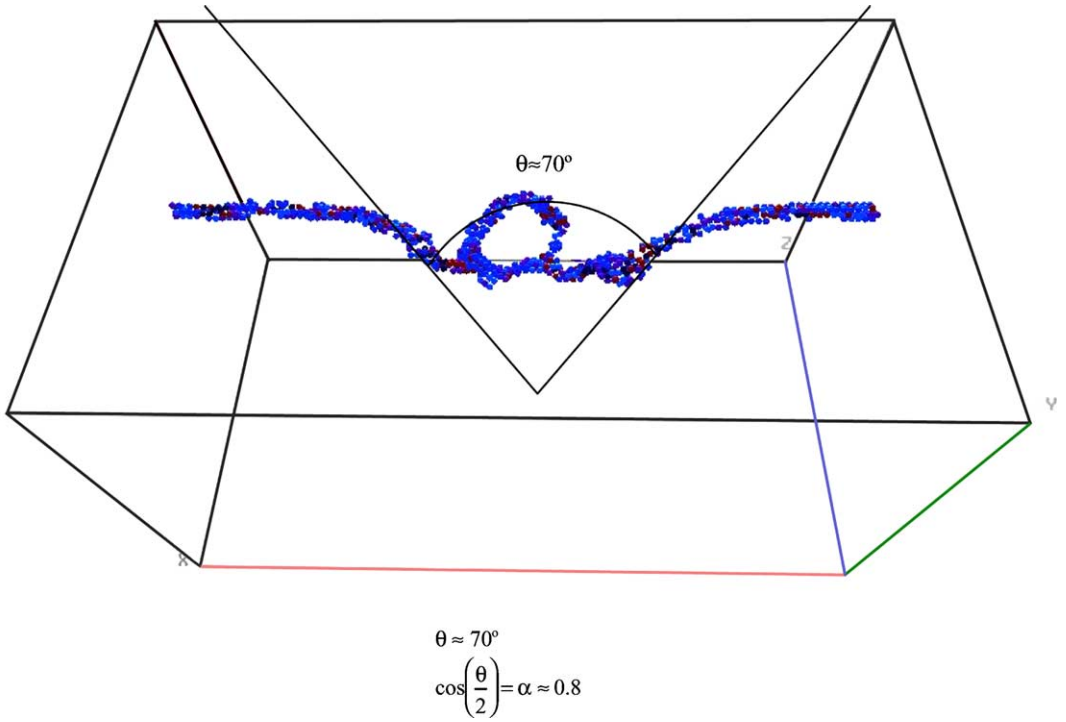

Fig. 7. Last snapshot before the dislocation breaks through the obstacle, leaving a [1 0 0] loop behind and two heavily curved spirals along the dislocation line. The critical angle is $\theta = 70°$, necessary to estimate the obstacle strength, $\alpha = \cos(\theta/2) = 0.82$.

the dislocation breaks free. From this value of θ, one can calculate the obstacle strength, $\alpha = \cos(\theta/2) = 0.82$. With this and $N = 1.2 \times 10^{23}$ m^{-3}, $d = 2$ nm and $K_a = 64$ GPa, [4] one can compute the change in shear stress, $\Delta\tau_s = 195$ MPa, due to Eq. (5). The computed value of α suggests a higher obstacle strength for $\langle 1\,0\,0\rangle$ loops than other calculations quoted in the literature [22,39]. Of course, N and d have been obtained directly from our computation box and are subject to the narrow applicability window of this MD simulation. N is unphysically high, with real values being two to three orders of magnitude lower. In addition, the product Nd inside the square root in Eq. (5) should in theory be an integral over the whole size spectrum. Further, it is not clear that the continuum line tension model used to calculate α is applicable at the atomic dimension. Therefore, our results are only intended to provide a first-order estimate of $\Delta\tau_s$.

In uniaxial, tensile loading conditions, the resolved shear stress for polycrystalline materials that slip on $\{1\,1\,0\}$ planes is related to the applied stress, σ_u, by [38]:

$$\sigma_u = T\tau_s, \tag{6}$$

where T is the Taylor factor and a standard value of 3.06 is commonly used for microstructure-mechanical property correlations [38]. Therefore, according to Eq. (6), we obtain $\Delta\sigma_u = 590$ MPa.

The calculations presented in this section suffer from obvious limitations. There is a strong statistical uncertainty associated with the single loop and interaction geometry considered, and to the conditions under which the simulations were performed. Also, the simulations have been carried out at strain rates that, although physically reasonable in some environments, are too high for the conditions expected in fusion steels. Our values of α and $\Delta\sigma_u$ are higher than those obtained experimentally or from other micromechanical estimations. α-values as high as 0.5 and 0.6 have been reported by Nicol et al. [22] and Hashimoto et al. [41], respectively, to describe yield stress changes of $\sim$200 and $\sim$450 MPa, but our predicted values of 0.8 and 600 MPa are about 50% too large. As well, α-values in the range of 0.5–0.8 must be considered suspect based on the standard value of $\sim$0.35 used to describe network dislocation reactions [42]. In any case, this work represents the first purely dynamical study of dislocation–obstacle interactions involving $\langle 1\,0\,0\rangle$ loops and screw dislocations in b.c.c. Fe and should be regarded as a first step in

[4] Instead of G, it is more appropriate to use K_a. K_a is related to the anisotropic shear modulus and is obtained from the modified elastic compliances [40].

estimating the relevant hardening parameters by computer simulation. Recently, similar works involving edge and screw dislocations interacting with voids and precipitates have been reported [19,28], and it is expected that the knowledge of dislocation–obstacle interactions will significantly increase as new techniques and potentials are being developed.

4. Summary and conclusions

A computational framework based on MD simulations to study hardening in fusion steels at low temperatures has been presented. The method briefly reviews the production of small $\frac{1}{2}\langle 1\,1\,1\rangle$ interstitial clusters in displacement cascades and describes the effect of dilute substitutional impurities on cluster migration, their interactions to form $\langle 1\,0\,0\rangle$ loops, and the interaction between these loops and $\frac{1}{2}\langle 1\,1\,1\rangle$ screw dislocations in b.c.c. Fe. In each step, direct comparison with experiments is provided when feasible.

Our results show that the presence of 1.0 at.% Cu in the b.c.c. lattice can enhance the 3D character of the clusters' migration and that the impact on cluster mobility can be explained by considering the displacement field interactions between the solute and self-interstitial cluster. This result can be extrapolated to suggest a strong and notable interaction for interstitial impurities and future computational efforts will be focused on further clarifying these interactions.

We have demonstrated that the $\langle 1\,0\,0\rangle$ junctions can form from the interaction of $\frac{1}{2}\langle 1\,1\,1\rangle$ self-interstitial clusters and that the energy landscape of the cluster junction should favor propagation throughout the cluster leading to the formation of small $\langle 1\,0\,0\rangle$ loops. Junction formation requires that both $\frac{1}{2}\langle 1\,1\,1\rangle$ loops have approximately the same shape and size, with $n > 20$ SIA, and that the clusters have intersecting glide prisms (Burger's vector) in accordance with Eq. (1). A growth mechanism for the formation of large $\langle 1\,0\,0\rangle$ loops has been identified, based on the biased absorption of small, cascade-produced $\frac{1}{2}\langle 1\,1\,1\rangle$ clusters. Further, we have obtained CTEM simulated images of these large $\langle 1\,0\,0\rangle$ loops by way of a multislice image simulation technique and compared them with real experimental micrographs to obtain good qualitative agreement.

To study the elementary hardening process in irradiated α-Fe, we have simulated the interaction between $\frac{1}{2}\langle 1\,1\,1\rangle$ screw dislocations and a large $\langle 1\,0\,0\rangle$ loop. At 750 MPa of applied stress and 100 K, the interaction results in a complex combination of dislocation loop segment absorption and pinning. The dislocation's structure becomes significantly altered, with large spiral segments being the dominant feature. When the stress is increased to 1.0 GPa, the dislocation releases from the $\langle 1\,0\,0\rangle$ loop at a critical angle of about 70°. These simulations permit calculation of the relevant parameters to estimate the hardening from Orowan's theory, most notably the obstacle strength of $\alpha = 0.82$. Our results overestimate experimental results by approximately a factor of two, which may be attributed to the limited scope in terms of time and space scales available to MD simulations or possibly the limited applicability of the continuum line tension model at the atomic level. Future work will further investigate the spectrum of dislocation–obstacle interactions and investigate the appropriate connection between the atomic mechanisms and continuum hardening relationships.

Acknowledgements

The authors are grateful to Drs W. Cai and V.V. Bulatov for their help with the implementation and MD simulations of screw dislocations. J.W. Rensman of the HFR facility at Petten provided the Fe–9Cr specimen for the TEM analysis. Useful discussions with Drs A. Caro, M. Victoria and P. Derlet are acknowledged. This work has been performed under the auspices of the US Department of Energy and Lawrence Livermore National Laboratory under contract W-7405-Eng-48 and within the CSN-UNESA Coordinated Research Programme under contract P000531499.

References

[1] E. Proust, L. Anzidi, G. Casini, M. Della Donne, L. Giancarli, S. Malang, Fusion Eng. Design 22 (1993) 19.
[2] K. Ehrlich, Phil. Trans. R. Soc. Lond. A 357 (1999) 595.
[3] M. Victoria, N. Baluc, P. Spätig, in: Proceedings of the 18th IAEA Fusion Energy Conference, Sorrento, Italy, 4–10 October 2000.
[4] J.M. Perlado, E. Domínguez, D. Lodi, L. Malerba, J. Marian, J. Prieto, M. Salvador, T. Díaz de la Rubia, E. Alonso, M.J. Caturla, L. Colombo, Fusion Technol. 39 (2001) 579.
[5] G.R. Odette, P. Lombrozo, Trans. Amer. Nucl. Soc. 44 (1983) 224.
[6] P.J. Karditsas, Fusion Eng. Design 48 (2000) 527.
[7] D.S. Gelles, M.L. Hamilton, R. Schäublin, in: S.T. Rosinski, M.L. Grossbeck, T.R. Allen, A.S. Kumar (Eds.), Effects of Radiation on Materials: 20th International Symposium, ASTM STP 1405, American Society for Testing and Materials, West Conshohocken, PA, 2002.
[8] R. Coppola, M. Magnani, R. May, A. Möslang, J. Appl. Crystallogr. 33 (2000) 469.
[9] A.E. Ward, S.B. Fisher, J. Nucl. Mater. 166 (1989) 227.
[10] K. Suganuma, H. Kayano, Radiat. Eff. 54 (1981) 81.
[11] B.C. Masters, Philos. Mag. 11 (1965) 881.
[12] E.A. Little, R. Bullough, M.H. Wood, Proc. Royal. Soc. Lond. A 372 (1980) 565.
[13] D.J. Bacon, T. Díaz de la Rubia, J. Nucl. Mater. 216 (1994) 275.

[14] Y.N. Osetsky, A. Serra, B.N. Singh, S.I. Golubov, Philos. Mag. A 80 (2000) 2131.
[15] N. Soneda, T. Díaz de la Rubia, Philos. Mag. A 78 (1998) 995.
[16] J. Marian, B.D. Wirth, J.M. Perlado, Phys. Rev. Lett. 88 (2002) 255507.
[17] R. Schäublin, A. Almazouzi, Y. Dali, Y.N. Osetsky, M. Victoria, J. Nucl. Mater. 276 (2000) 251.
[18] T. Harry, D.J. Bacon, Acta Mater. 50 (2002) 195; T. Harry, D.J. Bacon, Acta Mater. 50 (2002) 209.
[19] Y. Osetsky et al., these Proceedings.
[20] T. Díaz de la Rubia, M.W. Guinan, Mater. Res. Forum 174 (1990) 151.
[21] G.J. Ackland, D.J. Bacon, A.F. Calder, T. Harry, Philos. Mag. A 75 (1998) 713.
[22] A.C. Nicol, M.L. Jenkins, M.A. Kirk, Mater. Res. Soc. Symp. 650 (2001) R1.3.
[23] B.D. Wirth, G.R. Odette, D. Maroudas, G.E. Lucas, J. Nucl. Mater. 276 (2000) 33.
[24] B.L. Eyre, R. Bullough, Philos. Mag. 12 (1965) 31.
[25] S.M. Ohr, D.N. Beshers, Philos. Mag. 8 (1963) 1343; W. Carrington, K.F. Hale, D. McLean, Proc. Royal. Soc. Lond. A 259 (1960) 203.
[26] V.V. Bulatov, W. Cai, Phys. Rev. Lett. 89 (2002) 115501.
[27] Y.N. Osetsky, A. Serra, V. Priego, J. Nucl. Mater. 276 (2000) 202.
[28] J. Marian, PhD thesis, Universidad Politécnica de Madrid September, 2002.
[29] N. Soneda, S. Ishino, T. Diaz dela Rubia, in: Proceedings of the International Group on Radiation Damage Materials, 18–22 September 2000, Leuven, Belgium.
[30] J. Marian, B.D. Wirth, J.M. Perlado, G.R. Odette, T. Díaz de la Rubia, Phys. Rev. B 64 (2001) 094303.
[31] J. Marian, B.D. Wirth, A. Caro, B. Sadigh, G.R. Odette, J.M. Perlado, T. Díaz de la Rubia, Phys. Rev. B 65 (2002) 144102.
[32] B.D. Wirth, G.R. Odette, D. Maroudas, G.E. Lucas, J. Nucl. Mater. 244 (1997) 185.
[33] K. Arakawa, R. Imamura, K. Ohota, K. Ono, J. Appl. Phys. 89 (2001) 4752.
[34] M.J. Caturla et al., these Proceedings.
[35] J. Marian, B.D. Wirth, R. Schäublin, J.M. Perlado, T. Diaz de la Rubia, J. Nucl. Mater. 307–311 (2002) 871.
[36] P.A. Stadelmann, Ultramicroscopy 2 (1987) 131.
[37] R. Schäublin, Y. Dai, M. Victoria, in: H.A. Calderón Benavides, M.J. Yacamán (Eds.), Proceedings of the 14th International Congress on Electron Microscopy, vol. 1, Institute of Physics, Bristol and Philadelphia, 1998, p. 173.
[38] R.E. Stoller, S.J. Zinkle, J. Nucl. Mater. 283–287 (2000) 349.
[39] T. Takeyama, S. Ohnuki, H. Takahashi, Trans. Iron Steel Inst. Jpn. 21 (1981) 326.
[40] J.P. Hirth, J. Lothe, Theory of Dislocations, 2nd Ed., Krieger, 1982, p. 168.
[41] N. Hashimoto. S.J. Zinkle, R.L. Klueh, A.F. Rowcliffe, K. Shiba, in: G.E. Lucas, L. Snead, M.A. Kirk, R.G. Elliman (Eds.), Materials Research Society Symposium Proceedings, vol. 650, 2001, R1.10.
[42] P. Spätig, R. Schäublin, M. Victoria, in: H.N. Zbib, G.H. Campbell, M. Victoria, D.A. Hughes, L.E. Levine (Eds.), Materials Research Society Symposium Proceedings, vol. 683E, 2001, p. BB1.10.